Results in Physics 8 (2018) 268–275

Contents lists available at ScienceDirect

Results in Physics

journal homepage: www.journals.elsevier.com/results-in-physics

Three dimensional radiative flow of magnetite-nanofluid with homogeneous-heterogeneous reactions

Tasawar Hayat [a,b], Madiha Rashid [a,*], Ahmed Alsaedi [b]

[a] Department of Mathematics, Quaid-I-Azam University, 45320 Islamabad 44000, Pakistan
[b] Nonlinear Analysis and Applied Mathematics (NAAM) Research Group, Department of Mathematics, Faculty of Science, King Abdulaziz University, Jeddah 21589, Saudi Arabia

ARTICLE INFO

Article history:
Received 29 October 2017
Received in revised form 27 November 2017
Accepted 30 November 2017
Available online 9 December 2017

Keywords:
Nanofluid
MHD
Nonlinear radiation
Heat generation/absorption (nonuniform)
Homogeneous-heterogeneous reactions

ABSTRACT

Present communication deals with the effects of homogeneous-heterogeneous reactions in flow of nanofluid by non-linear stretching sheet. Water based nanofluid containing magnetite nanoparticles is considered. Non-linear radiation and non-uniform heat sink/source effects are examined. Non-linear differential systems are computed by Optimal homotopy analysis method (OHAM). Convergent solutions of nonlinear systems are established. The optimal data of auxiliary variables is obtained. Impact of several non-dimensional parameters for velocity components, temperature and concentration fields are examined. Graphs are plotted for analysis of surface drag force and heat transfer rate.

Introduction

Nanofluids are relatively new materials with suspension of nano-sized metallic or nonmetallic particles (1–100 nm). Nanofluids are dilute suspensions of functionalized nanomaterials with base fluids such as water, ethylene glycol etc. The nanofluid are considered useful in application such as engine cooling, drag reductions, domestic refrigerator chillers, electronic cooling, transformer cooling, nuclear systems cooling, oil engine transfer, boiler exhaust flue gas recovery, microwave tubes, diesel electric generator as jacket water coolant, high-power lasers, drilling, lubrications, cooling of welding, cooling and heating of buildings, thermal storage and solar water heating. Choi and Eastman [1] used metallic oxides nanoparticles for an enhancement of thermal conductivity. Heat transfer enhancement of nanofluids is studied by Xuan and Li [2]. Saidur et al. [3] presented a review about challenges and applications of nanofluids. Slip effects for silver and aluminium oxide nanofluid flow in a microchannel is presented by Karimipour et al. [4]. Hayat et al. [5] described flow of nanofluid past an exponential stretching with effects of thermal and solutal stratification. Zhang et al. [6] elaborated slip effects in time dependent power-law flow of nanofluid past a stretched sheet. Few more recent studies on nanofluids may include the (Refs. [7–15]).

Flow past a stretching surface in view of its significance related to industry and engineering fields. Such applications include condensation process of liquid films, glass fiber, paper production, crystal growing, plastic films and wires, polymer extrusion drawings and food manufacturing. Studies about linear stretching velocity has been widely discussed. Pioneer work on flow past a stretching surface was done by Crane [16]. Khan et al. [17] studied the three-dimensional flow of nanofluid over a nonlinear stretching sheet: An application to solar energy. Three-dimensional flow of nanofluid due to slendering stretching sheet with slip effect is discussed by Babu and Sandeep [18]. Mahanthesh et al. [19] presented a nonlinear radiative heat transfer in MHD three-dimensional flow of water based nanofluid over a non-linearly stretching sheet with convective boundary condition. MHD flow and nonlinear radiative heat transfer of Sisko nanofluid over a nonlinear stretching sheet is elaborated by Prasannakumara et al. [20].

Convective heat problems are significant in physical science within heat sources among the field. Applications related to energy problems including solidification of costing and cooling of underground electric cables are of great significance. Unsteady stretched flow with heat source/sink and thermal radiation is presented by Pal [21]. Ramandevi et al. [22] considered combined influence of viscous dissipation and non-uniform heat source/sink on MHD non-Newtonian fluid flow with non-Fourier heat flux model. Heat transfer control is important for final product of desired quality. Modern system of astrophysical flow, space vehicles, cooling of nuclear reactors, plasmas and electric power generation are

* Corresponding author.
E-mail address: madiha.rashid@math.qau.edu.pk (M. Rashid).

https://doi.org/10.1016/j.rinp.2017.11.038
2211-3797/

governed by applications of linear and nonlinear thermal radiation. Khan et al. [23] examined behavior of gyrotactic microorganisms and non-linear thermal radiation in flow of magneto-Burgers nanofluid. Peristaltic flow of nonconstant viscosity fluid with nonlinear thermal radiation is presented by Latif et al. [24]. Here impact of thermal radiation on electrical MHD flow of nanofluid over nonlinear stretching sheet with variable thickness discussed by Daniel et al. [25].

Homogeneous-heterogeneous reactions are natural processes of chemically reacting structures such as combustion, biochemical processes and catalysis. At different rates the relation among homogeneous-heterogeneous reactions along with consumption and production of reactant species within liquid and on catalytic surface is quite complicated. Some reactions have capacity to move slowly or not at all except in the existence of a catalyst. Applications of chemical reactions include manufacturing of food, formation and dispersion of fog, manufacturing of ceramics, production of polymer, crops damage via freezing, hydrometallurgical industry. Merkin [26] analyzed homogeneous-heterogeneous reactions in viscous fluid flow on a catalytic surface. Stagnation-point flow past a stretchable sheet in the presence of homogeneous-heterogeneous reactions are studied by Bachok et al. [27]. Gireesha et al. [28] describes three dimensional nonlinear flow of Casson-Carreau fluids with homogeneous and heterogeneous reactions. Nanofluid flow past a rotating disk of variable thickness and homogeneous-heterogeneous reactions is addressed by Hayat et al. [29]. Sajid et al. [30] presented influence of magnetohydrodynamics on Fe_3O_4-nanofluid with thermal radiation and homogeneous-heterogeneous reactions. Numerical study of silver and copper-water nanofluids with non-linear thermal radiation and homogeneous-heterogeneous reactions is due to Qayyum et al. [31].

Object of present communication is to analyze nonlinear radiative flow of magnetite nanofluid past a nonlinear stretching sheet. Effects of homogeneous-heterogeneous reactions are analyzed. Optimal homotopy analysis technique (OHAM) [32–40] is initialized for convergent series solutions of physical quantities. The residual errors are shown through numerical data. Graphical results are used to elaborate the impacts of involved parameters.

Mathematical modeling

Three-dimensional flow of viscous nanofluid is examined. Flow caused by nonlinearly stretching sheet with velocities $\breve{u}_w = c(x+y)^n$ and $\breve{v}_w = d(x+y)^n$ (n being the power-law index) (see Fig. 1). Contribution due to non-uniform heat source/sink and non-linear radiation are studied. Applied magnetic field of strength $\widetilde{B}_0$ acts transversely to flow. Omission of electric and induced magneticfield is ensured. Homogeneous-heterogeneous reactions of two typical chemical species A and B have been analyzed. Homogeneous reactions for cubic autocatalysis are

$$A + 2B \to 3B, \quad \text{rate} = \kappa_c \breve{a}\breve{b}^2, \tag{1}$$

while on catalyst surface the required heterogenous reactions is

$$A \to B, \quad \text{rate} = \kappa_e \breve{a}, \tag{2}$$

where rate constants are κ_c and κ_e and A and B are rate of chemical species having concentrations $\breve{a}$ and $\breve{b}$.

The problem statements are

$$\frac{\partial \breve{u}}{\partial x} + \frac{\partial \breve{v}}{\partial y} + \frac{\partial \breve{w}}{\partial z} = 0, \tag{3}$$

$$\rho_{nf}\left(\breve{u}\frac{\partial \breve{u}}{\partial x} + \breve{v}\frac{\partial \breve{u}}{\partial y} + \breve{w}\frac{\partial \breve{u}}{\partial z}\right) = \mu_{nf}\left(\frac{\partial^2 \breve{u}}{\partial z^2}\right) - \sigma_{nf}\widetilde{B}_0^2\breve{u}, \tag{4}$$

$$\rho_{nf}\left(\breve{u}\frac{\partial \breve{v}}{\partial x} + \breve{v}\frac{\partial \breve{v}}{\partial y} + \breve{w}\frac{\partial \breve{v}}{\partial z}\right) = \mu_{nf}\left(\frac{\partial^2 \breve{v}}{\partial z^2}\right) - \sigma_{nf}\widetilde{B}_0^2\breve{v}, \tag{5}$$

$$(\rho Cp)_{nf}\left(\breve{u}\frac{\partial \breve{T}}{\partial x} + \breve{v}\frac{\partial \breve{T}}{\partial y} + \breve{w}\frac{\partial \breve{T}}{\partial z}\right) = k_{nf}\frac{\partial^2 \breve{T}}{\partial z^2} - \frac{1}{(\rho C_p)_{nf}}\frac{\partial q_{\hbar}}{\partial z} + Q''', \tag{6}$$

$$\breve{u}\frac{\partial \breve{a}}{\partial x} + \breve{v}\frac{\partial \breve{a}}{\partial y} + \breve{w}\frac{\partial \breve{a}}{\partial z} = D_A\frac{\partial^2 \breve{a}}{\partial z^2} - \kappa_c\breve{a}\breve{b}^2, \tag{7}$$

$$\breve{u}\frac{\partial \breve{b}}{\partial x} + \breve{v}\frac{\partial \breve{b}}{\partial y} + \breve{w}\frac{\partial \breve{b}}{\partial z} = D_B\frac{\partial^2 \breve{b}}{\partial z^2} + \kappa_c\breve{a}\breve{b}^2, \tag{8}$$

$$\begin{aligned} &\breve{u} = \breve{u}_w = c(x+y)^n, \ \breve{v} = \breve{v}_w = d(x+y)^n, \ \breve{w} = 0, \ \breve{T} = \breve{T}_w, \\ &D_A\frac{\partial \breve{a}}{\partial z} = k_e\breve{a}, \ D_B\frac{\partial \breve{b}}{\partial z} = -k_e\breve{a} \text{ at } z = 0, \\ &\breve{u} \to 0, \ \breve{v} \to 0, \ \breve{a} \to \breve{a}_0, \ \breve{T} \to \breve{T}_\infty, \ \breve{b} \to 0, \quad \text{as } z \to \infty, \end{aligned} \tag{9}$$

where (x, y, z) components of velocity are $(\breve{u}, \breve{v}, \breve{w})$, $\breve{T}$ temperature, ρ the fluid density, σ fluid electrical conductivity and D_A and D_B the diffusion coefficients respectively.

Here effective dynamic viscosity of nanofluid is

$$\mu_{nf} = \frac{\mu_f}{(1-\phi)^{2.5}}. \tag{10}$$

Heat capacitance $(\rho C_p)_{nf}$, the effective density ρ_{nf}, effective thermal conductivity k_{nf} and thermal diffusivity α_{nf} of nanofluid are

$$\alpha_{nf} = \frac{k_{nf}}{(\rho C_p)_{nf}}, \ \rho_{nf} = (1-\phi)\rho_f + \phi\rho_s, \ (\rho C_p)_{nf} = (1-\phi)(\rho C_p)_f + \phi(\rho C_p)_s, \tag{11}$$

where ϕ the solid and spherical volume fraction of nanoparticles magnetite (Fe_3O_4), C_p the specific heat, k_f the thermal conductivity, k_{nf} the effective thermal conductivity and s and f in subscript are for

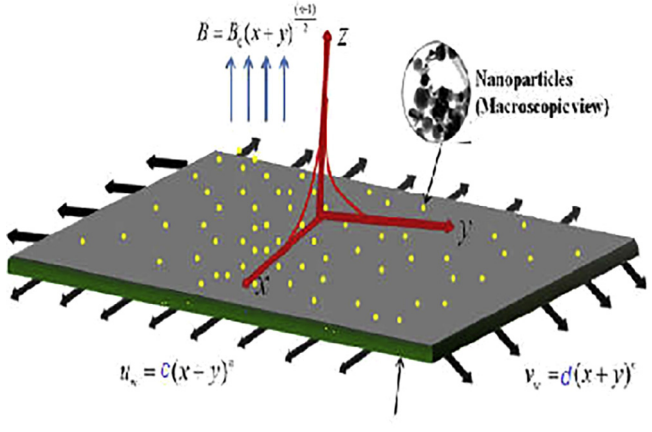

Fig. 1. Flow geometry.

Table 1
Thermophysical properties of magnetite (Fe_3O_4) and water.

	$k(W/mk)$	$\rho(kg/m^3)$	$\sigma(Um)^{-1}$	$C_p(J/kgk)$
(Fe_3O_4)	9.7	5180	25000	670
Water (H_2O)	0.613	997.1	0.05	4179

nano-solid particles and base fluid of the nanofluid. Thermophysical properties of nanofluid are displayed in Table 1.

Maxwell mode of effective thermal conductivity and effective electrical conductivity are

$$\frac{k_{nf}}{k_f}=\frac{(k_s+2k_f)-2\phi(k_f-k_s)}{(k_s+2k_f)-2\phi(k_f-k_s)},$$
$$\frac{\sigma_{nf}}{\sigma_f}=1+\frac{3\left(\frac{\sigma_s}{\sigma_f}-1\right)\phi}{\left(\frac{\sigma_s}{\sigma_f}+2\right)-\left(\frac{\sigma_s}{\sigma_f}-1\right)\phi}. \tag{12}$$

Utilizing the Rosseland concept for radiative heat flux we have

$$q_{\breve{h}}=-\frac{4\sigma^*\partial\breve{T}^4}{3\mathbb{k}^*\partial z}=-\frac{16\sigma^*}{3\mathbb{k}^*}\breve{T}^3\frac{\partial\breve{T}}{\partial z}, \tag{13}$$

where σ^* and $\mathbb{k}^*$ stands for Stefan–Boltzmann and Rosseland mean absorption coefficients. Eq. (6) is reduced to

$$(\rho Cp)_{nf}\left(\breve{u}\frac{\partial\breve{T}}{\partial x}+\breve{v}\frac{\partial\breve{T}}{\partial y}+\breve{w}\frac{\partial\breve{T}}{\partial z}\right)=k_{nf}\left(\frac{\partial^2\breve{T}}{\partial z^2}\right)+\frac{1}{(\rho C_p)_f}\frac{16\sigma^*}{3\mathbb{k}^*}\frac{\partial}{\partial z}\left(\breve{T}^3\frac{\partial\breve{T}}{\partial z}\right)-Q'''. \tag{14}$$

For non-uniform heat source/sink) are

$$Q'''=\left(\frac{k_f u_w(z)}{z\nu_f}\right)\left[I_1*\left(\breve{T}_w-\breve{T}_\infty\right)\tilde{f}'(\xi)+I_2\left(\breve{T}-\breve{T}_\infty\right)\right] \tag{15}$$

where I_1 and I_2 are the heat generation/absorption coefficients respectively.

Considering

$$\breve{u}=c(x+y)^n\tilde{f}'(\xi),\ \breve{v}=d(x+y)^n\tilde{g}'(\xi),\ \xi=z\sqrt{\left(\frac{n+1}{2}\right)\frac{c}{\nu_f}(x+y)^{n-1}},$$
$$\breve{w}=-\sqrt{\left(\frac{n+1}{2}\right)\nu_f c(x+y)^{n-1}}\left[\left(\tilde{f}+\tilde{g}\right)+\frac{n-1}{n+1}\xi\left(\tilde{f}'+\tilde{g}'\right)\right],$$
$$\tilde{\vartheta}(\xi)=\frac{\breve{T}-\breve{T}_\infty}{\breve{T}_w-\breve{T}_\infty},\breve{a}=\breve{a}\tilde{j}(\xi),\breve{b}=\breve{b}\tilde{s}(\xi). \tag{16}$$

Eqs. (3)–(5), (7)–(9) and (14) take the form

$$\left(\frac{1}{(1-\phi)^{2.5}(1-\phi+\phi\frac{\rho_s}{\rho_f})}\right)\tilde{f}'''+\left(\tilde{f}+\tilde{g}\right)\tilde{f}''-\frac{2n}{n+1}\left(\tilde{f}'+\tilde{g}'\right)\tilde{f}'-Ma\frac{\left(\frac{\sigma_{nf}}{\sigma_f}\right)}{(1-\phi+\phi\frac{\rho_s}{\rho_f})}\tilde{f}'=0, \tag{17}$$

$$\left(\frac{1}{(1-\phi)^{2.5}(1-\phi+\phi\frac{\rho_s}{\rho_f})}\right)\tilde{g}'''+\left(\tilde{f}+\tilde{g}\right)\tilde{g}''-\frac{2n}{n+1}\left(\tilde{f}'+\tilde{g}'\right)\tilde{g}'-Ma\frac{\left(\frac{\sigma_{nf}}{\sigma_f}\right)}{(1-\phi+\phi\frac{\rho_s}{\rho_f})}\tilde{g}'=0, \tag{18}$$

$$\left(\frac{1}{1-\phi+\phi\frac{(\rho C_\rho)_s}{(\rho C_\rho)_f}}\right)\left(\frac{k_{nf}}{k_f}+Rd\right)\left(\frac{1}{\Pr}\right)\tilde{\vartheta}''+\left(\frac{1}{1-\phi+\phi\frac{(\rho C_\rho)_s}{(\rho C_\rho)_f}}\right)\left(\frac{1}{\Pr}\right)\left(I_1\tilde{f}'+I_2\tilde{\vartheta}\right)+\left(\frac{Rd}{\left(1-\phi+\phi\frac{(\rho C_\rho)_s}{(\rho C_\rho)_f}\right)}\right)\left(\frac{1}{\Pr}\right)\begin{bmatrix}\left(\tilde{\vartheta}_w-1\right)^3\left(3\tilde{\vartheta}^2\tilde{\vartheta}'^2+\tilde{\vartheta}^3\tilde{\vartheta}''\right)\\+3\left(\tilde{\vartheta}_w-1\right)^2\left(2\tilde{\vartheta}\tilde{\vartheta}'^2+\tilde{\vartheta}^2\tilde{\vartheta}''\right)\\+3\left(\tilde{\vartheta}_w-1\right)\left(\tilde{\vartheta}'^2+\tilde{\vartheta}\tilde{\vartheta}''\right)\end{bmatrix}+\left(\tilde{f}+\tilde{g}\right)\tilde{\vartheta}'=0, \tag{19}$$

$$\left(\frac{1}{Sc}\right)\tilde{j}''+\left(\tilde{f}+\tilde{g}\right)\tilde{j}'-\frac{2}{n+1}K^*\tilde{j}\tilde{s}^2=0, \tag{20}$$

$$\left(\frac{\epsilon}{Sc}\right)\tilde{s}''+\left(\tilde{f}+\tilde{g}\right)\tilde{s}'+\frac{2}{n+1}K^*\tilde{j}\tilde{s}^2=0, \tag{21}$$

$$\tilde{f}(0)=0,\tilde{f}'(0)=1,\tilde{f}'(\infty)=0,\tilde{f}''(\infty)=0,$$
$$\tilde{g}(0)=0,\tilde{g}'(0)=\alpha,$$
$$\tilde{\vartheta}(0)=1,\tilde{\vartheta}(\infty)=0, \tag{22}$$

$$\tilde{j}'(0)=\sqrt{\frac{2}{n+1}}K^s\tilde{j}(0),\tilde{j}(\infty)\to 1,$$
$$\epsilon\tilde{s}'(0)=-\sqrt{\frac{2}{n+1}}K^s\tilde{j}(0),\tilde{s}(\infty)\to 1. \tag{23}$$

Here we make an assumption that diffusion coefficients for both chemical species are same i.e. $\epsilon=1$ and thus

$$\tilde{j}(\eta)+\tilde{s}(\eta)=1 \tag{24}$$

Eqs. (20) and (21) yield

$$\left(\frac{1}{Sc}\right)\tilde{j}''+\left(\tilde{f}+\tilde{g}\right)\tilde{j}'-\frac{2}{n+1}K^*\tilde{j}\left(1-\tilde{j}\right)^2=0, \tag{25}$$

with the boundary condition

$$\tilde{j}'(0)=\sqrt{\frac{2}{n+1}}K^s\tilde{j}(0),\tilde{j}(\infty)=1. \tag{26}$$

Here magnetic parameter Ma, velocity ratio parameter α, radiation parameter Rd, temperature parameter $\tilde{\theta}w$, Prandtl number Pr, Schmidt number Sc, Diffusion ratio coefficient ϵ, homogeneous reaction strength K^* and heterogenous reaction strength K^s are defined as follows:

$$Ma=\frac{\sigma_f B_0^2}{\rho_f c},\alpha=\frac{d}{c},Rd=\frac{16\sigma^*\breve{T}_\infty^3}{3k_f k^*},\theta w=\frac{\breve{T}_f}{\breve{T}_\infty},\Pr=\frac{\upsilon_f\left(\mu\breve{C}_p\right)_f}{k_f},$$
$$Sc=\frac{\nu_f}{D_A},\epsilon=\frac{D_B}{D_A},K^*=\frac{k_c\breve{a}}{c(x+y)^{n-1}},K^s=\frac{k_e}{D_A}\sqrt{\frac{\upsilon_f}{c(x+y)^{n-1}}}. \tag{27}$$

Here skin-friction coefficient (C_f and C_g) and local Nusselt number (Nu) are

$$C_f=\frac{\tau_{wx}}{\frac{1}{2}\rho_f\breve{u}_w^2},C_g=\frac{\tau_{wy}}{\frac{1}{2}\rho_f\breve{u}_w^2},Nu=-\frac{(x+y)q_w}{k_{nf}\left(\breve{T}_w-\breve{T}_\infty\right)}, \tag{28}$$

$$\tau_{\breve{w}x}=\mu_{nf}\left(\frac{\partial\breve{u}}{\partial z}+\frac{\partial\breve{w}}{\partial x}\right)_{z=0},\tau_{\breve{w}y}=\mu_{nf}\left(\frac{\partial\breve{v}}{\partial z}+\frac{\partial\breve{w}}{\partial y}\right)_{z=0},$$
$$q_{\breve{w}}=-k_{nf}\mu_{nf}\frac{\partial\breve{T}}{\partial z_{z=0}}+\left(q_{\breve{h}}\right)_{\breve{w}}=-\left(\breve{T}_w-\breve{T}_\infty\right)\sqrt{\frac{c}{\upsilon_f}}(1+Rd\tilde{\vartheta}_w^3)\tilde{\vartheta}'(0). \tag{29}$$

Dimensionless expressions of C_f, C_g, and Nu are

$$\mathrm{Re}_x^{1/2}C_f=\frac{1}{(1-\phi)^{2.5}}\tilde{f}''(0),\mathrm{Re}_x^{1/2}C_g=\frac{1}{(1-\phi)^{2.5}}\tilde{g}''(0),$$
$$\mathrm{Re}_x^{-1/2}Nu=-\frac{n+1}{2}\left[1+\frac{4}{3}Rd(1+(\tilde{\vartheta}_w-1))(\tilde{\vartheta}(0))^3\right]\tilde{\vartheta}'(0), \tag{30}$$

in which $\mathrm{Re}_x=c(x+b)/\nu$ denotes the local Reynolds number.

Optimal homotopic solutions

The optimal similar series solutions of Eqs. (17)–(19) and (25) with boundary conditions (22) and (26) are established by using optimal homotopy analysis technique (OHAM). We select suitable operators and initial guesses as follows:

$$\tilde{f}_0(\xi)=1-\exp(-\xi),\tilde{g}_0(\xi)=\alpha(1-\exp(-\xi)),$$
$$\tilde{\vartheta}_0(\xi)=\exp(-\xi),\tilde{j}=1-\frac{1}{2}\exp(-\sqrt{\frac{2}{n+1}}K^s(\xi), \tag{31}$$

with

$$\mathcal{L}_{\tilde{f}} = \tilde{f}''' - \tilde{f}', \mathcal{L}_{\tilde{g}} = \tilde{g}'' - \tilde{g}, \mathcal{L}_{\tilde{\vartheta}} = \tilde{\vartheta}'' - \tilde{\vartheta}, \mathcal{L}_{\tilde{j}} = \tilde{j}'' - \tilde{j}, \tag{32}$$

and

$$\begin{aligned} \mathcal{L}_{\tilde{f}}[\dot{d}_1 + \dot{d}_2 \exp(\xi) + \dot{d}_3 \exp(-\xi)] &= 0, \\ \mathcal{L}_{\tilde{g}}[\dot{d}_4 \exp(\xi) + \dot{d}_5 \exp(-\xi)] &= 0, \\ \mathcal{L}_{\tilde{\vartheta}}[\dot{d}_6 \exp(\xi) + \dot{d}_7 \exp(-\xi)] &= 0, \\ \mathcal{L}_{\tilde{j}}[\dot{d}_8 \exp(\xi) + \dot{d}_9 \exp(-\xi)] &= 0, \end{aligned} \tag{33}$$

in which $\dot{d}_i$ $(i = 1{-}9)$ depict the arbitrary constants. Computations of zeroth and mth order deformation problems are done with BVPh2.0 of Mathematica.

Optimal convergence analysis

In homotopic solutions the non-zero auxiliary variables $\hbar_{\tilde{f}}$, $\hbar_{\tilde{g}}, \hbar_{\tilde{\vartheta}}$ and $\hbar_{\tilde{j}}$ ensures convergence analysis. For optimal data of

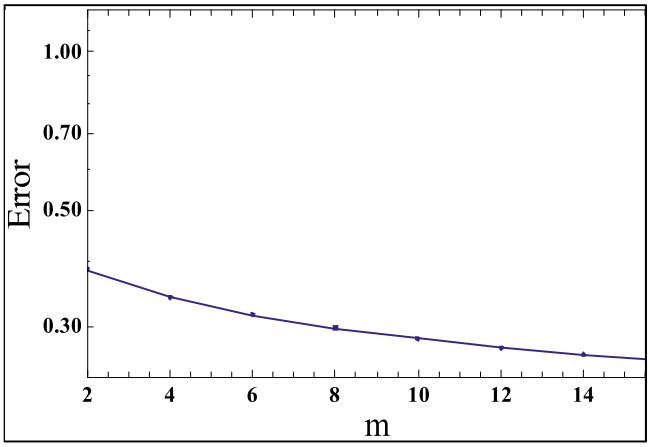

Fig. 2. Total reidual error for Fe_3O_4 nanofluid.

$\hbar_{\tilde{f}}, \hbar_{\tilde{g}}, \hbar_{\tilde{\vartheta}}$ and $\hbar_{\tilde{j}}$, we have applied concept of minimization by considering averaged squared residual errors as suggested by Liao [32].

$$\varrho_m^{\breve{f}} = \frac{1}{k+1}\sum_{l=0}^{k}\left[\mathcal{N}_{\breve{f}}\left(\sum_{i=0}^{m}\breve{f}(\xi), \sum_{i=0}^{m}\breve{g}(\xi)\right)_{\xi=l\delta\xi}\right]^2, \tag{34}$$

$$\varrho_m^{\breve{g}} = \frac{1}{k+1}\sum_{l=0}^{k}\left[\mathcal{N}_{\breve{g}}\left(\sum_{i=0}^{m}\breve{f}(\xi), \sum_{i=0}^{m}\breve{g}(\xi)\right)_{\xi=l\delta\xi}\right]^2, \tag{35}$$

$$\varrho_m^{\breve{\vartheta}} = \frac{1}{k+1}\sum_{l=0}^{k}\left[\mathcal{N}_{\breve{\vartheta}}\left(\sum_{i=0}^{m}\breve{f}(\xi), \sum_{i=0}^{m}\breve{g}(\xi), \sum_{i=0}^{m}\breve{\vartheta}(\xi)\right)_{\xi=l\delta\xi}\right]^2, \tag{36}$$

$$\varrho_m^{\breve{j}} = \frac{1}{k+1}\sum_{l=0}^{k}\left[\mathcal{N}_{\breve{j}}\left(\sum_{i=0}^{m}\breve{f}(\xi), \sum_{i=0}^{m}\breve{g}(\xi), \sum_{i=0}^{m}\breve{j}(\xi)\right)_{\xi=l\delta\xi}\right]^2. \tag{37}$$

Following

$$\varrho_m^{t} = \varrho_m^{\breve{f}} + \varrho_m^{\breve{g}} + \varrho_m^{\breve{\vartheta}} + \varrho_m^{\breve{j}}, \tag{38}$$

where ϱ_m^t represents total squared residual error, $\delta\xi = 0.5$ and $k = 16$. For magnetite-water the convergence control parameter have optimal values like $h_{\tilde{f}} = -0.686258, h_{\tilde{g}} = 0.651312$, $h_{\tilde{\vartheta}} = -0.112385$ and $h_{\tilde{j}} = -1.92267$ and total average squared residual error is $\varrho_m^t = 0.384779$ taken at 2nd order of approximations. For Fe_3O_4-water the total residual error is plotted in Fig. 2. By using optimal values of $\hbar$ the averaged squared residual errors at $m = 2$ for Fe_3O_4-water is shown in Table 2. Noted that averaged squared residual errors show decreasing trend for higher order deformations. Table 3 provides comparison of skin friction coefficient. The results are found in good agreement.

Physical interpretation

This portion includes behaviors of velocity, temperature, concentration, skin friction coefficient and heat transfer rate for various involved parameters.

Table 2
Individual averaged squared residual errors having optimal values of auxiliary variables for Fe_3O_4-Water.

m	$\varepsilon_m^{\breve{f}}$	$\varepsilon_m^{\breve{g}}$	$\varepsilon_m^{\breve{\vartheta}}$	$\varepsilon_m^{\breve{j}}$
2	2.97942×10^{-4}	4.38213×10^{-5}	9.50986×10^{-5}	3.84342×10^{-1}
4	6.50099×10^{-5}	8.08571×10^{-6}	5.50189×10^{-5}	3.41095×10^{-1}
6	2.97292×10^{-5}	3.2684×10^{-6}	3.85403×10^{-5}	3.15708×10^{-1}
8	1.72782×10^{-5}	1.68369×10^{-6}	2.97053×10^{-5}	2.97885×10^{-1}
10	1.13359×10^{-5}	9.92329×10^{-7}	2.42156×10^{-5}	2.84327×10^{-1}
12	8.03415×10^{-6}	6.40412×10^{-7}	2.04679×10^{-5}	2.73598×10^{-1}
14	6.00804×10^{-6}	4.41266×10^{-7}	1.77406×10^{-5}	2.65008×10^{-1}
16	4.67339×10^{-6}	3.19449×10^{-7}	1.56633×10^{-5}	2.58267×10^{-1}

Table 3
Comparison of the values of skin friction coefficient when $M = I_1 = I_2 = K^* = K^s = 0$ and variation of ϕ.

n	α	ϕ	Junaid [17]		Mahantesh [19]		Present study	
			$-f''(0)$	$-g''(0)$	$-f''(0)$	$-g''(0)$	$-f''(0)$	$-g''(0)$
$n \geqslant 1$	0	0	1.62435	0	1.62436	0	1.6243	0
$n \geqslant 1$	0.5	0	1.98942	0.99471	1.98942	0.99471	1.98947	0.99477
$n \geqslant 1$	1	0	2.29718	2.29718	2.29718	2.29719	2.29712	2.29715
$n \geqslant 1$	0.1	0.05	–	–	2.20611	1.10306	2.20611	1.10306
$n \geqslant 1$	0.1	0.1	–	–	2.33707	1.16853	2.33711	1.16850
$n \geqslant 1$	0.1	0.2	–	–	2.4232	1.2116	2.4238	1.2113

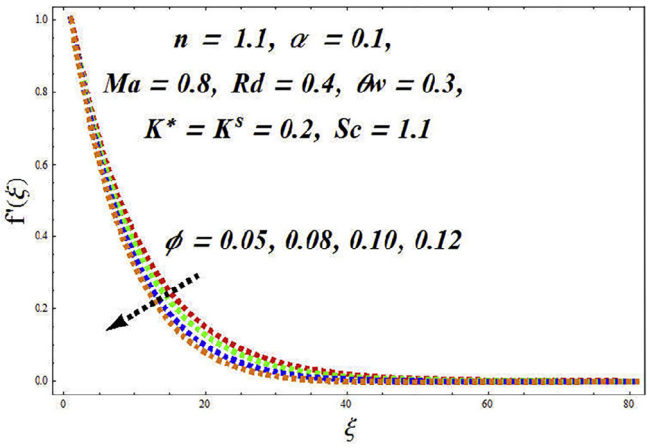

Fig. 3. $\tilde{f}'(\xi)$ for ϕ variation.

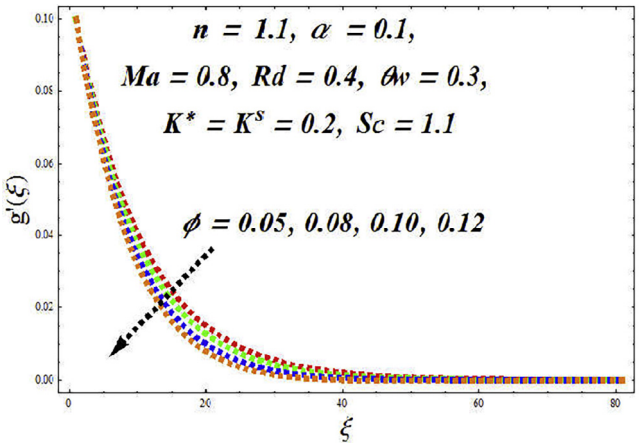

Fig. 4. $\tilde{g}'(\xi)$ for ϕ variation.

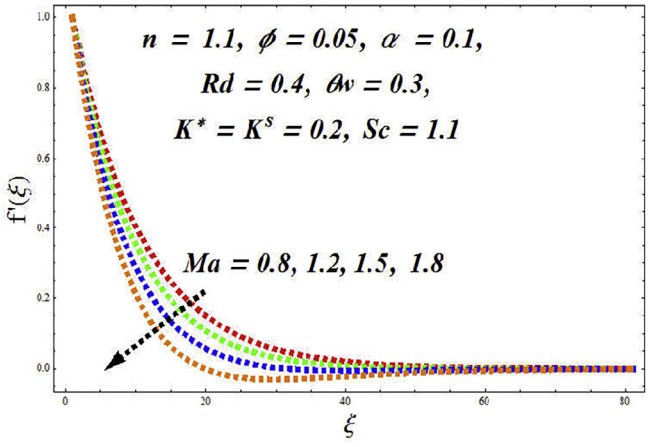

Fig. 5. $\tilde{f}'(\xi)$ for *Ma* variation.

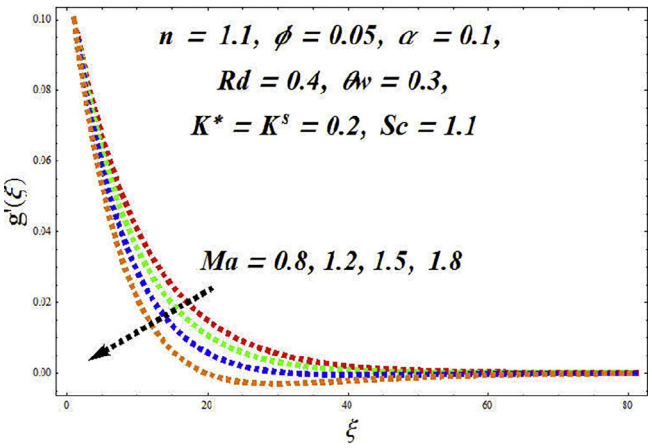

Fig. 6. $\tilde{g}'(\xi)$ for *Ma* variation.

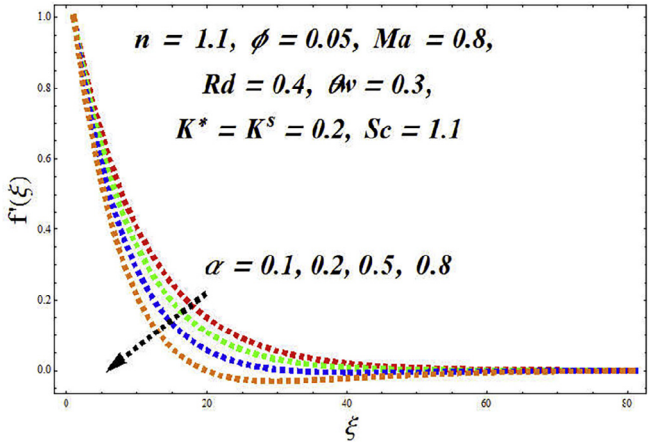

Fig. 7. $\tilde{f}'(\xi)$ for α variation.

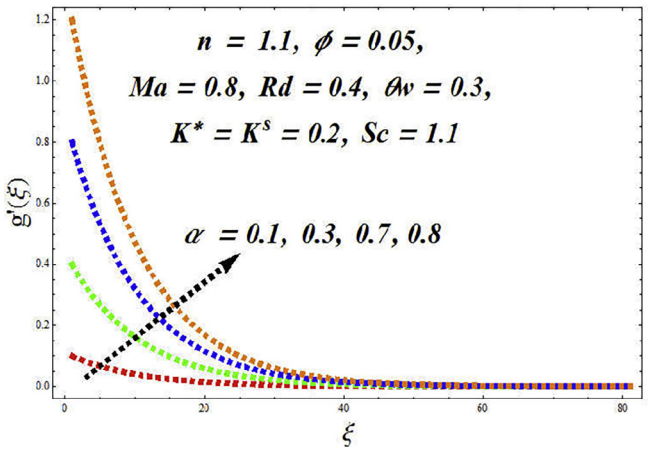

Fig. 8. $\tilde{g}'(\xi)$ for α variation.

Dimensionless velocity

Figs. 3 and 4 illustrate the effect of ϕ on velocities $\tilde{f}'(\xi)$ and $\tilde{g}'(\xi)$. A decline in velocity is observed for positive values of ϕ. Physically the resistance between the fluid particles enhances for larger ϕ which produce a decreasing trend in velocities $\tilde{f}'(\xi)$ and $\tilde{g}'(\xi)$. Figs. 5 and 6 are sketched to indicate the behavior of magnetic parameter *Ma* for velocities $\tilde{f}'(\xi)$ and $\tilde{g}'(\xi)$. Here decline in velocities are subject to increasing values of *Ma*. It is observed that drag force (which is known as Lorentz force) is created by iApplication of magnetic-field. This force has ability to slow down flow. Figs. 7 and 8 are plotted to examine variation of velocities (along *x* and *y* directions)

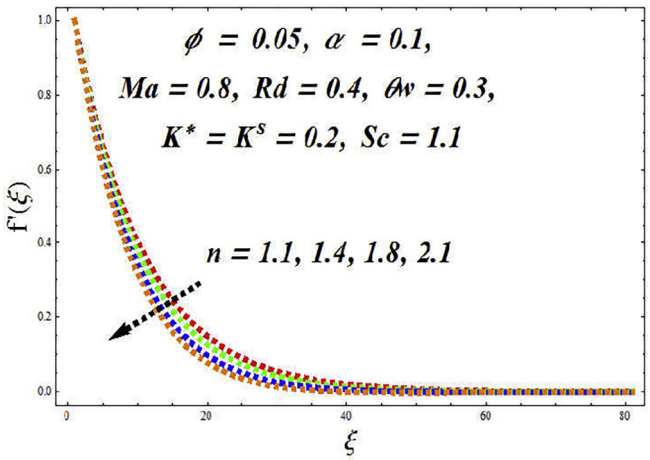

Fig. 9. $\tilde{f}'(\xi)$ for n variation.

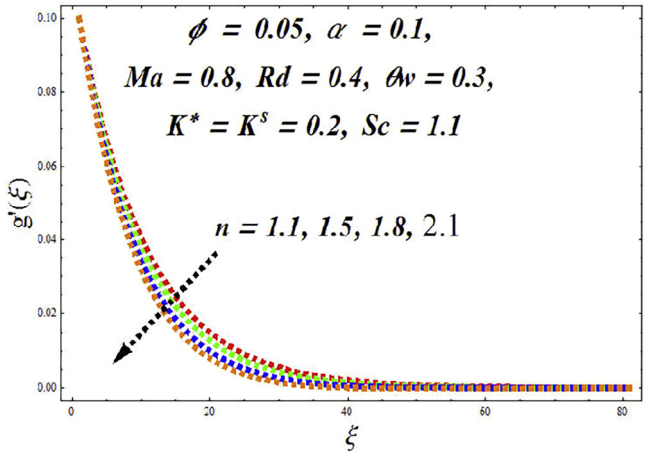

Fig. 10. $\tilde{g}'(\xi)$ for n variation.

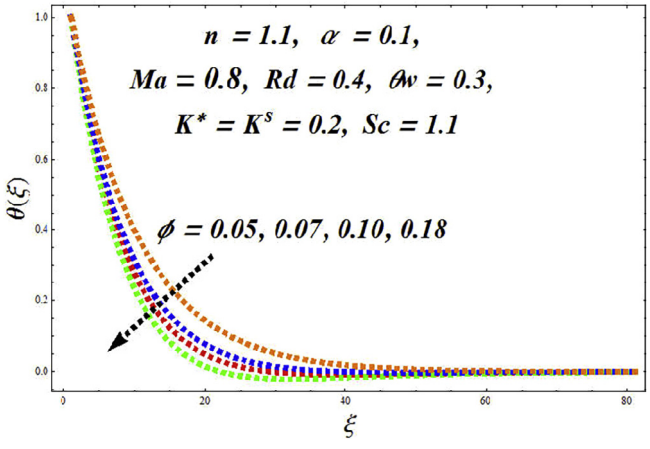

Fig. 11. $\tilde{\theta}(\xi)$ for ϕ variation.

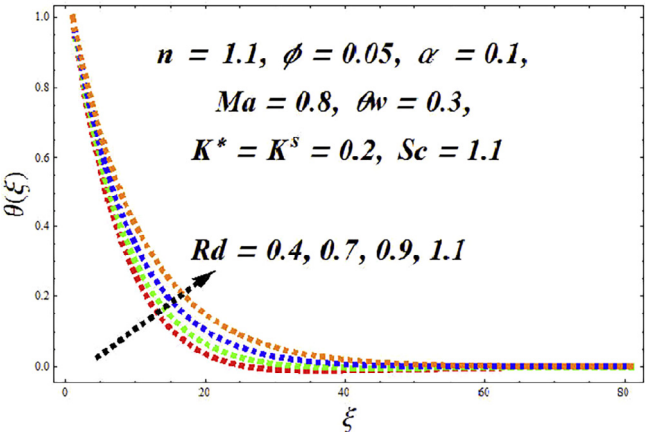

Fig. 12. $\tilde{\theta}(\xi)$ for Rd variation.

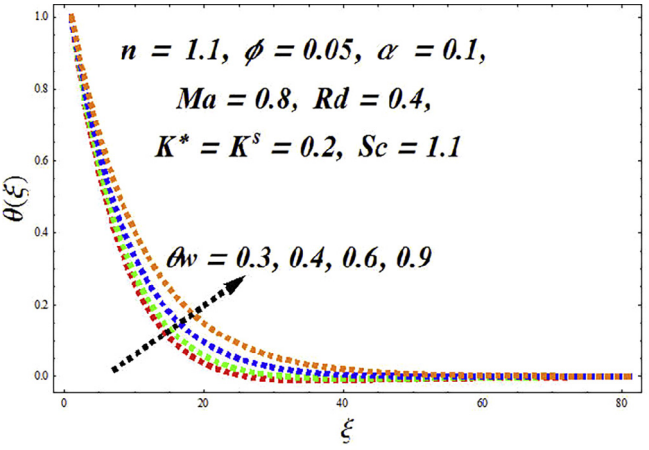

Fig. 13. $\tilde{\theta}(\xi)$ for θw variation.

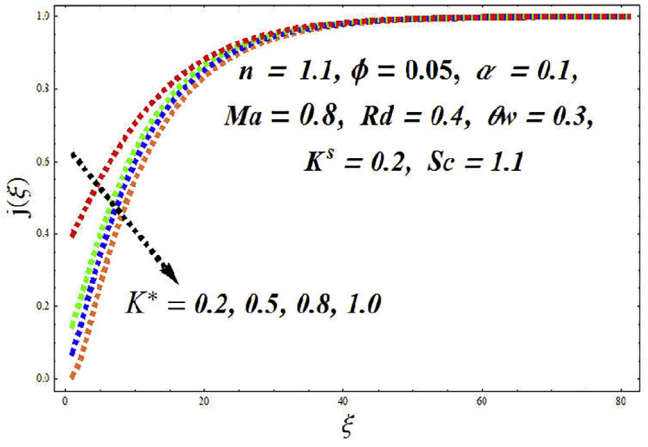

Fig. 14. $\tilde{j}(\xi)$ for K^* variation.

respectively for larger α. Higher values of α constitute larger velocity field along y-direction while opposite trend can be observed for velocity field along x-direction. Physically larger values of $\alpha = \frac{d}{c}$ leads to either increase in d or decrease in c, the velocity along x -direction decreased and velocity along y-direction increased correspondingly. For higher values of power-law index n, the velocities and momentum boundary layer thickness reduces (see Figs. 9 and 10).

Temperature

Influence of nanoparticles volume fraction ϕ on $\tilde{\theta}(\xi)$ is displayed in Fig. 11. Rising behavior of thermal field and associated layer thickness is noted via ϕ. Thermal boundary layer concept to

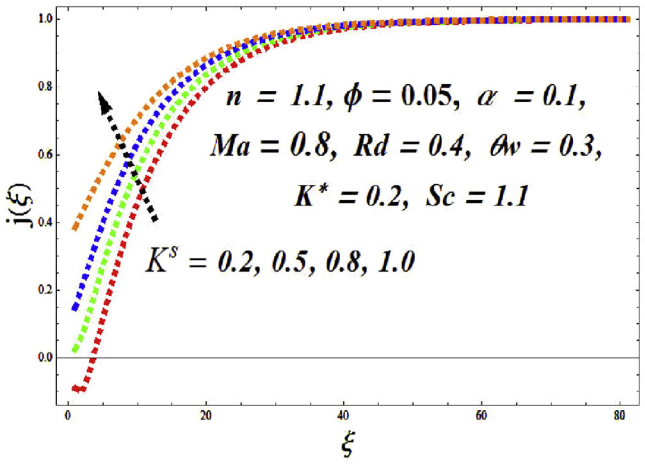

Fig. 15. $\tilde{j}(\xi)$ for K^s variation.

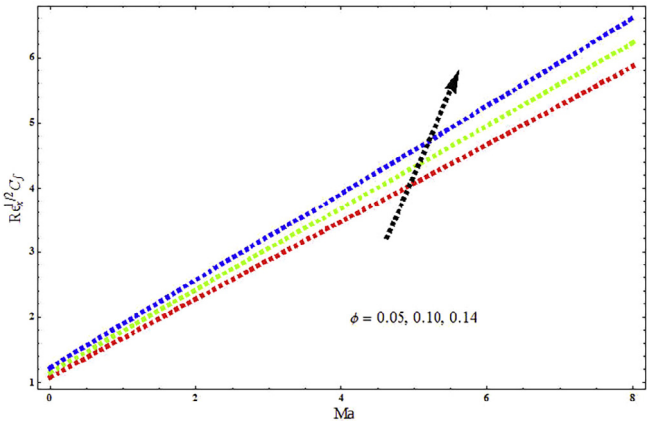

Fig. 16. $C_f(Re_x)^{\frac{1}{2}}$ for ϕ variation.

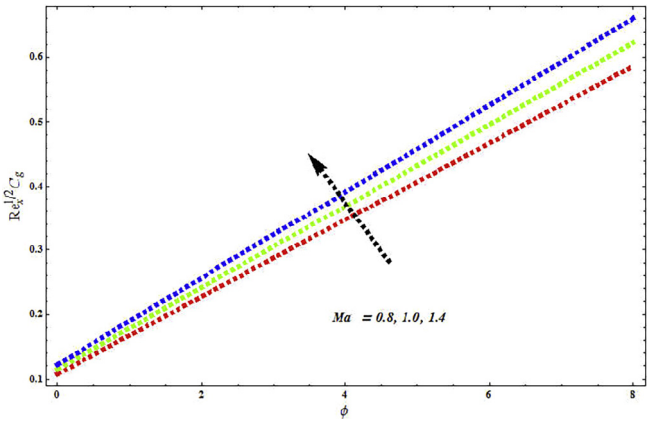

Fig. 17. $C_g(Re_x)^{\frac{1}{2}}$ for Ma variation.

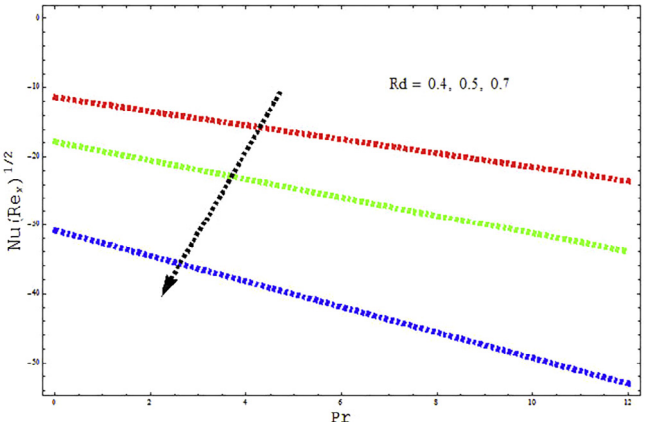

Fig. 18. $Nu(Re_x)^{-\frac{1}{2}}$ for Rd variation.

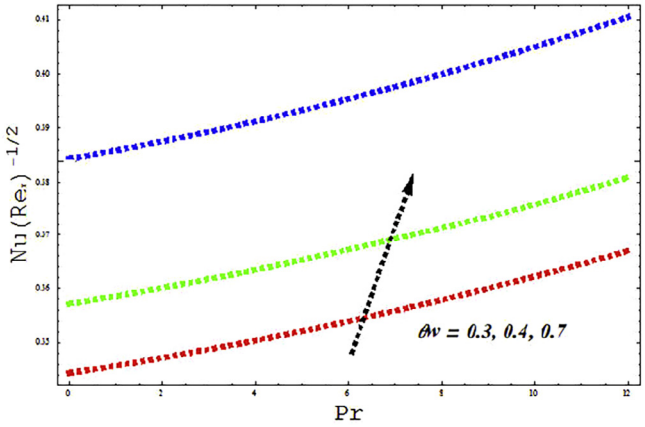

Fig. 19. $Nu(Re_x)^{-\frac{1}{2}}$ for θw variation.

nanoparticles volume fraction is in accordance with an increment of thermal conductivity of nanoliquid. Fig. 12 shows Rd effect on $\tilde{\theta}(\xi)$. Both thermal field and associated layer thickness are increasing functions of Rd. Physically it is verified because of radiation process in working fluid the heat is created which rises fluid's temperature. Effects of temperature ratio parameter θw on $\tilde{\theta}(\xi)$ is displayed in Fig. 13. It can be seen from figure that an increment in θw increases the fluid thermal state which is responsible for the higher temperature.

Concentration

Impact of homogeneous reaction parameter K^* on concentration $\tilde{j}(\xi)$ is analyzed in Fig. 14. When homogeneous reaction parameter enhanced, concentration distribution $\tilde{j}(\xi)$ reduces due to consumption of reactions. Behavior of heterogeneous reaction parameter K^s on the concentration is displayed in Fig. 15. For higher values of K^s the diffusion reduces and less diffused nanoparticles enhances $\tilde{j}(\xi)$.

Skin friction coefficient and local Nusselt number

Figs. 16–19 show the graph of skin-friction coefficients (C_f and C_g) and local Nusselt number (Nu) for volume fraction of nanomaterial, magnetic parameter, radiation parameter and temperature parameter respectively. Skin friction coefficient depicts increasing behavior via ϕ and Ma (see Figs. 16 and 17). Fig. 18 shows that magnitude of heat transfer rate enhances against Rd. For higher θw the local Nusselt number enhances (see in Fig. 19).

Conclusions

Main points are as follows:

- Velocity field retards for magnetic parameter while it rises for velocity ratio parameter.
- Impact of nanoparticles volume fraction for momentum and thermal layers is opposite
- For fluid concentration the strength of heterogenous reaction variable rises while opposite is noticed for homogeneous reaction case.
- Skin friction coefficient increases for magnetic parameter and nanoparticles volume fraction.
- Magnitude of radiation and temperature ratio parameter on local Nusselt number are qualitatively similar.

References

[1] Choi SUS, Eastman JA. Enhancing thermal conductivity of fluids with nanoparticles ASME Int. Mech Eng Cong Expo 1995;66:99–105.
[2] Xuan Y, Li Q. Heat transfer enhancement of nanofluids. Int J Heat Fluid Flow 2000;21:58–64.
[3] Saidur R, Leong KY, Mohammad HA. A review on applications and challenges of nanofluids. Renewable Sustainable Energy Rev. 2011;15:1646–68.
[4] Karimipour A, D'Orazio A, Shadloo MS. The effects of different nano particles of Al_2O_3 and Ag on the MHD nano fluid flow and heat transfer in a microchannel including slip velocity and temperature jump. Phy E Low-dim Sys Nanostruct 2017;86:146–53.
[5] Hayat T, Rashid M, Imtiaz M, Alsaedi A. MHD effects on a thermo-solutalstratified nanofluid flow on an exponentially radiating stretching sheet. J App Mech Tech Phys 2017;58:214–23.
[6] Zhang Y, Zhang M, Bai Y. Unsteady flow and heat transfer of power-law nanofluid thin film over a stretching sheet with variable magnetic field and power-law velocity slip effect. J Taiwan Inst Chem Eng 2017;70:104–10.
[7] Hayat T, Imtiaz M, Alsaedi A, Kutbi MA. MHD three-dimensional flow of nanofluid with velocity slip and nonlinear thermal radiation. J Magn Magn Mater 2015;396:31–7.
[8] Hayat T, Waqas M, Khan MI, Alsaedi A. Analysis of thixotropic nanomaterial in a doubly stratified medium considering magnetic field effects. Int J Heat Mass Transfer 2016;102:1123–9.
[9] Sheikholeslami M, Bhatti MM. Forced convection of nanofluid in presence of constant magnetic field considering shape effects of nanoparticles. Int J Heat Mass Transfer 2017;111:1039–49.
[10] Waqas M, Khan MI, Hayat T, Alsaedi A. Numerical simulation for magneto Carreau nanofluid model with thermal radiation: a revised model. Comp Methods App Mech Eng 2017;432:640–53.
[11] Irfan M, Khan M, Khan WA. Numerical analysis of unsteady 3D flow of Carreau nanofluid with variable thermal conductivity and heat source/sink. Res Phys 2017;7:3315–24.
[12] Sheikholeslami M, Hayat T, Alsaedi A. Numerical study for external magnetic source influence on water based nanofluid convective heat transfer. Int J Heat Mass Transfer 2017;106:745–55.
[13] Khan WA, Irfan M, Khan M, Alshomrani AS, Alzahrani AK, Alghamdi MS. Impact of chemical processes on magneto nanoparticle for the generalized Burgers fluid. J Mol Liq 2017;234:201–8.
[14] Hayat T, Saleem A, Tanveer A, Alsaadi F. Numerical analysis for peristalsis of Williamson nanofluid in presence of an endoscope. Int J Heat Mass Transfer 2017;114:395–401.
[15] Sheikholeslami M, Hayat T, Alsaedi A. On simulation of nanofluid radiation and natural convection in an enclosure with elliptical cylinders. Int J Heat Mass Transfer 2017;114:981–91.
[16] Crane LJ. Flow past a stretching plate. ZAMP 1970;21(6):45–647.
[17] Khan JA, Mustafa M, Hayat T, Alsaedi A. Three-dimensional flow of nanofluid over a nonlinear stretching sheet: An application to solar energy. Int J Heat Mass Transfer 2015;86:158–64.
[18] Babu MJ, Sandeep N. Three-dimensional MHD slip flow of nanofluids over a slendering stretching sheet with thermophoresis and Brownian motion effects. Adv Powder Tech 2016:2039–50.
[19] Mahanthesh B, Gireesha BJ, Gorla RSR. Nonlinear radiative heat transfer in MHD three-dimensional flow of water based nanofluid over a non-linearly stretching sheet with convective boundary condition. J Nigerian Math Soc 2016;35:178–98.
[20] Prasannakumara BC, Gireesha BJ, Krishnamurthy MR, Kumar KG. MHD flow and nonlinear radiative heat transfer of Sisko nanofluid over a nonlinear stretching sheet. Inf Med Unlocked 2017;9:123–32.
[21] Pal D. Combined effects of no-uniform heat source/sink and thermal radiation on heat transfer over an unsteady permeable surfaces. Commun Nonlinear Sci Numer Simul 2011;16:1890–940.
[22] Ramandevia B, Reddy JVR, Sugunamma V, Sandeep N. Combined influence of viscous dissipation and non-uniform heat source/sink on MHD non-Newtonian fluid flow with Cattaneo-Christov heat flux. Alex Eng J 2017. https://doi.org/10.1016/j.aej.2017.01.026.
[23] Khan M, Irfan M, Khan WA. Impact of nonlinear thermal radiation and gyrotactic microorganisms on the Magneto-Burgers nanofluid. Int J Mech Sci 2017;130:375–82.
[24] Latif T, Alvi N, Hussain Q, Asghar S. Peristaltic flow of nonconstant viscosity fluid with nonlinear thermal radiation. J Comput Theor Nanosci 2017;14:2681–93.
[25] Daniel YS, Aziz ZA, Ismail Z, Salah F. Impact of thermal radiation on electrical MHD flow of nanofluid over nonlinear stretching sheet with variable thickness. Alex Eng J 2017. https://doi.org/10.1016/j.aej.2017.07.007.
[26] Merkin JH. A model for isothermal homogeneous-heterogeneous reactions in boundary layer flow. Math Comp Model 1996;24:125–36.
[27] Bachok N, Ishak A, Pop I. On the stagnation-point flow towards a stretching sheet with homogeneous—heterogeneous reactions effects. Commun Nonlinear Sci Numer Simul 2011;16:4296–302.
[28] Gireesha BJ, Kumar PBS, Mahanthesh B, Shehzad SA, Rauf A. Nonlinear 3D flow of Casson-Carreau fluids with homogeneous–heterogeneous reactions: a comparative study. Res Phys 2017;7:2762–70.
[29] Hayat T, Rashid M, Imtiaz M, Alsaedi A. Nanofluid flow due to rotating disk with variable thickness and homogeneous-heterogeneous reactions. Int J Heat Mass Transfer 2017;113:96–105.
[30] Sajid M, Iqbal SA, Naveed M, Abbas Z. Effect of homogeneous-heterogeneous reactions and magnetohydrodynamics on Fe3O4 nanofluid for the Blasius flow with thermal radiations. J Mol Liq 2017:115–21.
[31] Qayyum S, Khan MI, Hayat T, Alsaedi A. A framework for nonlinear thermal radiation and homogeneous-heterogeneous reactions flow based on silver-water and copper-water nanoparticles: A numerical model for probable error. Res Phys 2017;7:1907–14.
[32] Liao SJ. An optimal homotopy-analysis approach for strongly nonlinear differential equations. Commun Nonlinear Sci Numer Simul 2010;15:2003–16.
[33] Hayat T, Shehzad SA, Alsaed A. Soret and Dufour Effects on MHD Flow of Casson Fluid. Appl Math Mech 2012;33:1301–12.
[34] Hayat T, Shehzad SA, Qasim M, Obaidat S. Radiative flow of Jeffery fluid in a porous medium with power law heat flux and heat source. Nucl Eng Des 2012;243:15–9.
[35] Awais M, Saleem S, Hayat T, Irum S. Hydromagnetic couple-stress nanofluid flow over a moving convective wall: OHAM analysis. Acta Astronaut 2016;129:271–6.
[36] Hayat T, Muhammad T, Shehzad SA, Alsaedi A. Three dimensional rotating flow of Maxwell nanofluid. J Mol Liq 2017;229:495–500.
[37] Khan M, Irfan M, Khan WA. Impact of nonlinear thermal radiation and gyrotactic microorganisms on the Magneto-Burgers nanofluid. Int J Mech Sci 2017;130:375–82.
[38] Hayat T, Rashid M, Alsaedi A. MHD convective flow of magnetite-Fe3O4 nanoparticles by curved stretching sheet. Res Phys 2017;7:3107–15.
[39] Waqas M, Hayat T, Shehzad SA, Alsaedi A. Transport of magnetohydrodynamic nanomaterial in a stratified medium considering gyrotactic microorganisms. Physica B 2018;529:33–40.
[40] Gupta S, Kumar D, Singh J. MHD mixed convective stagnation point flow and heat transfer of an incompressible nanofluid over an inclined stretching sheet with chemical reaction and radiation. Int J Heat Mass Transfer 2018;118:378–87.